

# Study of the reaction $\gamma p \rightarrow K^+ \Lambda(1520)$ at photon energies up to 2.65 GeV\*

F. W. Wieland<sup>1,4</sup>, J. Barth<sup>1</sup>, K.-H. Glander<sup>1,6</sup>, J. Hannappel<sup>1</sup>, N. Jöpen<sup>1</sup>, F. Klein<sup>1,a</sup>, E. Klempt<sup>2</sup>, R. Lawall<sup>1,7</sup>, D. Menze<sup>1</sup>, M. Ostrick<sup>3</sup>, E. Paul<sup>1</sup>, I. Schulday<sup>1,5</sup>, W. J. Schuille<sup>1</sup>

<sup>1</sup> Physikalisches Institut der Universität Bonn, Germany

<sup>2</sup> Helmholtz-Institut für Strahlen- und Kernphysik, Universität Bonn, Germany

<sup>3</sup> Institut für Kernphysik, Universität Mainz, Germany

<sup>4</sup> presently Wieland KG, Lüdenscheid, Germany

<sup>5</sup> presently IFB AG, Köln, Germany

<sup>6</sup> presently TRW Automotive GmbH, Alfdorf, Germany

<sup>7</sup> presently TÜV Nord, Germany

Received: date / Revised version: date

**Abstract.** The reaction  $\gamma p \rightarrow K^+ \Lambda(1520)$  was measured in the energy range from threshold to 2.65 GeV with the SAPHIR detector at the electron stretcher facility ELSA in Bonn. The  $\Lambda(1520)$  production cross section was analyzed in the decay modes  $pK^-$ ,  $n\bar{K}^0$ ,  $\Sigma^\pm\pi^\mp$ , and  $\Lambda\pi^+\pi^-$  as a function of the photon energy and the squared four-momentum transfer  $t$ . While the cross sections for the inclusive reactions rise steadily with energy, the cross section of the process  $\gamma p \rightarrow K^+ \Lambda(1520)$  peaks at a photon energy of about 2.0 GeV, falls off exponentially with  $t$ , and shows a slope flattening with increasing photon energy. The angular distributions in the  $t$ -channel helicity system indicate neither a  $K$  nor a  $K^*$  exchange dominance. The interpretation of the  $\Lambda(1520)$  as a  $\Sigma(1385)\pi$  molecule is not supported.

**PACS.** 13.30.-a Decays of baryons – 14.20.Jn hyperons

## 1 Introduction

We report on a study of the dynamics of the process  $\gamma p \rightarrow K^+ \Lambda(1520)$  for photon energies from threshold to 2.65 GeV. The CLAS collaboration [1] investigated this process in electroproduction, at electron beam energies of 4.05, 4.25, and 4.46 GeV, in the kinematic region spanning the squared momentum transfer  $Q^2$  from 0.9 to 2.4 GeV<sup>2</sup> and for invariant masses  $W$  from 1.95 to 2.65 GeV, and suggested that the reaction is dominated by  $t$ -channel processes. From a comparison between their  $t$ -channel helicity-frame angular distributions and angular distributions from photoproduction measured at Daresbury for photon energies from 2.8 to 4.8 GeV [2], the CLAS collaboration concluded that  $t$ -channel diagrams with longitudinally polarized photons contribute significantly to electroproduction of  $\Lambda(1520)$ . Here we present new photoproduction results in a  $W$  range below the Daresbury data, allowing for a better comparison with CLAS.

The  $\Lambda(1520)$  production was investigated in the decay channels  $\Lambda(1520) \rightarrow pK^-$ ,  $n\bar{K}_s^0$ ,  $\Sigma^\pm\pi^\mp$ , and  $\Lambda\pi^+\pi^-$ . We present, in four energy bins, total cross sections, differential cross sections  $d\sigma/dt$  and angular distributions in

the  $t$ -channel helicity system.  $\Lambda$  decay fractions and an upper limit for the fractional contribution of  $\Lambda(1520) \rightarrow \Sigma(1385)\pi$  in the  $\Lambda\pi^+\pi^-$  final state are reported. The results presented here are based on 180 million triggers which were taken with the SAPHIR detector. A study of the related reactions  $\gamma p \rightarrow K^+ \Sigma^\pm\pi^\mp$  can be found in an accompanying paper [3]. The data are available via internet.<sup>1</sup>

## 2 The experiment

The SAPHIR detector is a magnetic multiparticle spectrometer [4] which took data at the 3.5 GeV electron stretcher facility ELSA [5]. The setup is shown schematically in fig. 1. An extracted electron beam of 2.8 GeV was directed on a radiator target to provide an energy-tagged photon beam within the range from 0.868 GeV to 2.650 GeV. The data-taking was based on a trigger defined by a coincidence of signals from the scattered electrons in the tagging system with at least two charged particles in the scintillator hodoscopes, and no signal from a beam veto counter downstream of SAPHIR which detected non-interacting photons. The drift chambers served to measure charged

\* This work is supported in part by the Deutsche Forschungsgemeinschaft (SPP KL 980/2-3) and the SFB/TR16

<sup>a</sup> E-mail: klein@physik.uni-bonn.de

<sup>1</sup> <http://saphir.physik.uni-bonn.de/saphir/publications>

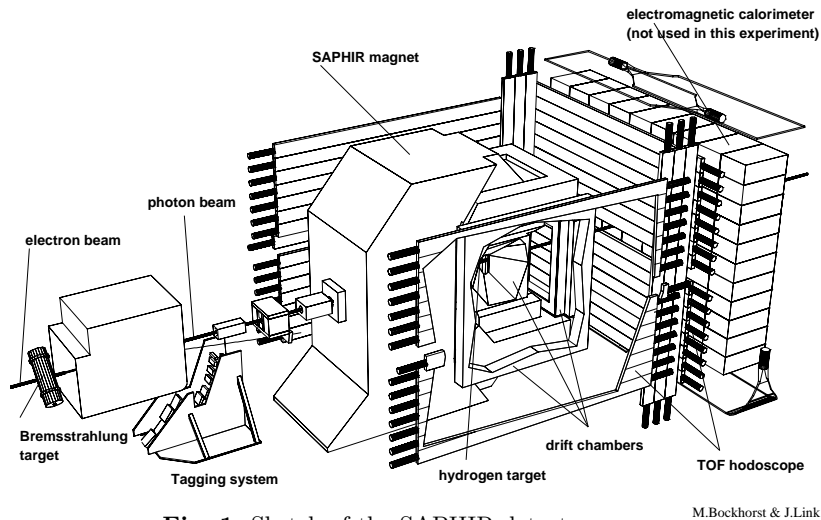


Fig. 1. Sketch of the SAPHIR detector.

particle tracks. The scintillator hodoscopes were used for time-of-flight (TOF) measurements and in order to determine the particle masses from the track momentum (measured with the drift chambers in the magnetic field). For a more detailed description see [6, 7].

### 3 Event reconstruction and event selection

#### 3.1 $\Lambda(1520) \rightarrow pK^-$

Events from the reaction  $\gamma p \rightarrow K^+ p K^-$  were selected from three-track events via a kinematic fit using the measured photon energy in the tagging system and the momenta of the charged particles. Events were accepted, if the fit probability  $P(\chi^2)$  was larger than those of competing reactions (see table 1) and larger than 0.001, and if the mass assignments of the charged particles were in accordance with the time-of-flight measurement in the scintillator hodoscopes. In order to achieve a better signal to background ratio, events from the reaction  $\gamma p \rightarrow p\phi$  with  $\phi$  decays into  $K^+ K^-$  were removed for photon energies above 1.93 GeV by a cut in the  $K^+ K^-$  mass distribution ( $1.0097 \text{ GeV} < M_{K^+ K^-} < 1.0285 \text{ GeV}$ ).

Figure 2 shows the  $pK^-$  invariant mass distributions for the full photon energy range (left panel) and for four energy bins (right panel). The distributions show a strong  $\Lambda(1520)$  signal. The  $\Lambda(1520)$  contribution was separated from the background by fitting a polynomial of fifth order together with an appropriate signal function. For this signal function a convolution of a Breit-Wigner shape with natural decay width and of two Gaussians, reflecting the experimental resolution (so-called double Voigt function), was used. These fits were carried out with mass and width of  $\Lambda(1520)$  fixed to PDG values [8].

#### 3.2 $\Lambda(1520) \rightarrow nK_s^0$

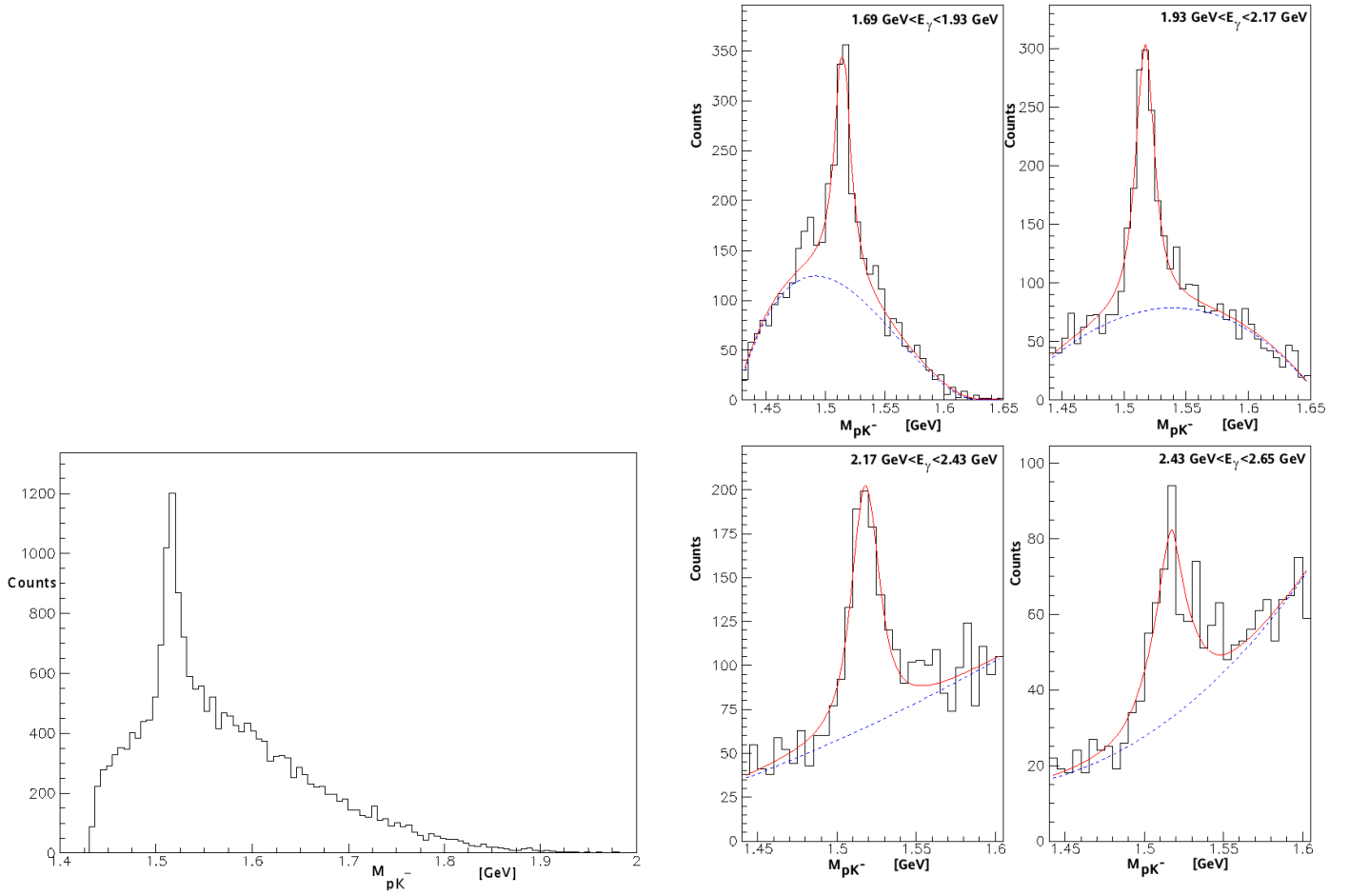
The topology of the reaction  $\gamma p \rightarrow K^+ n K_s^0$ , where  $K_s^0$  decays into  $\pi^+ \pi^-$ , is shown in fig. 3(a). The secondary

Table 1. Reaction hypotheses used for kinematic fitting.

Hypothesis	Reaction
1	$\gamma p \rightarrow p K^+ K^-$
2	$\gamma p \rightarrow K^+ K_s^0 n$
3	$\gamma p \rightarrow K^+ \Sigma^+ \pi^-$
4	$\gamma p \rightarrow K^+ \Sigma^- \pi^+$
5	$\gamma p \rightarrow p \pi^+ \pi^-$
6	$\gamma p \rightarrow p \pi^+ \pi^- \pi^0$
7	$\gamma p \rightarrow n \pi^+ \pi^- \pi^+$
8	$\gamma p \rightarrow p K_s^0 K_L^0$
9	$\gamma p \rightarrow K_s^0 \Sigma^+$
10	$\gamma p \rightarrow K^+ \Lambda \pi^0$
11	$\gamma p \rightarrow K_s^0 \Lambda \pi^+$
12	$\gamma p \rightarrow K_s^0 \Sigma^+ \pi^0$
13	$\gamma p \rightarrow K^+ \Lambda$
14	$\gamma p \rightarrow K^+ \Sigma^0$
15	$\gamma p \rightarrow K_L^0 \Lambda \pi^+$

vertex of the  $K_s^0$  decay was reconstructed by a fit. Vertices with a total charge of zero and an invariant mass near the  $K_s^0$  mass ( $|M_{\pi^+ \pi^-} - M_{K_s^0}| < 0.03 \text{ GeV}$ ) were selected. Using time-of-flight information it was checked that the mass of the positive decay-particle is compatible with the pion mass. In addition it was required that the mass of the second positively charged particle is compatible with the mass of the  $K^+$ , in the mass range from 0.4 GeV to 0.7 GeV. The primary vertex was determined by a vertex fit including the  $K^+$  track and the line of flight of the  $K_s^0$ . Events with a neutron in the final state were selected by a cut on the missing mass recoiling against the  $K^+ K_s^0$  system ( $|M_{\text{miss}} - M_n| < 0.07 \text{ GeV}$ ).

Finally a kinematic fit was used to distinguish between the wanted reaction and other channels (see table 1). Remaining background from the reactions  $\gamma p \rightarrow K^+ \Sigma^\pm \pi^\mp$ , which can populate the same final state, was removed by



**Fig. 2.** Reaction  $\gamma p \rightarrow pK^+K^-$ : Invariant mass distribution of the  $pK^-$  system with the peak of the  $\Lambda(1520)$  (left) and invariant mass distribution of the  $pK^-$  system in four energy intervals (right panel).

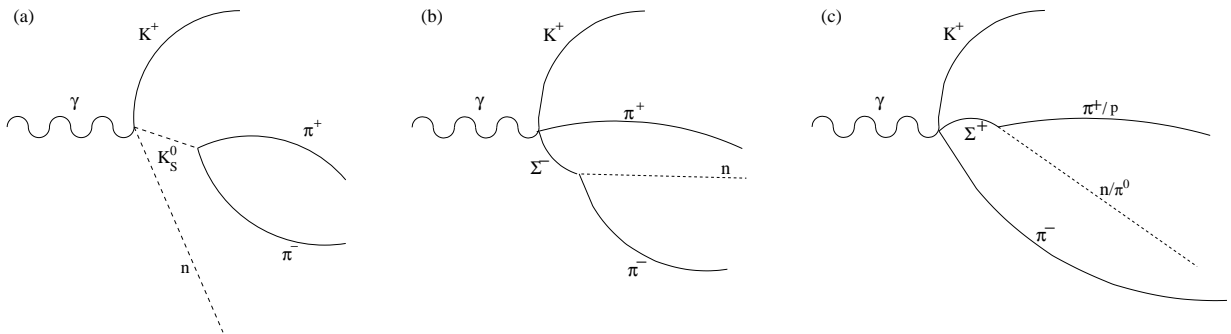


**Fig. 3.** Topology of the reactions  $\gamma p \rightarrow K^+K_s^0n$  (a),  $\gamma p \rightarrow K^+\Sigma^-\pi^+$  (b) and  $\gamma p \rightarrow K^+\Sigma^+\pi^-$  (c).

a cut on the invariant  $n\pi^\pm$  mass in the range  $1.180 \text{ GeV} < M_{n\pi^+} < 1.210 \text{ GeV}$  and  $1.180 < M_{n\pi^-} < 1.204 \text{ GeV}$ , respectively.

Figure 4(a) shows the invariant mass distribution of  $\pi^+\pi^-$  pairs with the  $K_s^0$  peak, after preselection of the events, fig. 4(b) the missing mass distribution calculated for the unmeasured neutral particles with the neutron peak. In fig. 5, after the final event selection, the following distributions are presented: (a) the invariant mass distribution

of  $\pi^+\pi^-$  pairs from  $K_s^0$  decay, (b) the  $K_s^0$  decay time distribution and, in fig. 6, the  $K_s^0n$  mass distribution with the  $\Lambda(1520)$  peak.

The  $\pi^+\pi^-$  mass distribution in fig. 4(a) was fitted assuming a Gaussian shape, giving a  $K^0$  mass of  $(0.497 \pm 0.0003) \text{ GeV}$  in agreement with the nominal value [8]. Also the decay time distribution in fig. 5(b) with  $\tau = (0.84 \pm 0.04) \cdot 10^{-10} \text{ s}$  is consistent with the nominal value. Similar to the  $pK^-$  case, the  $\Lambda(1520)$  peak was fitted in the  $nK_s^0$  mass dis-

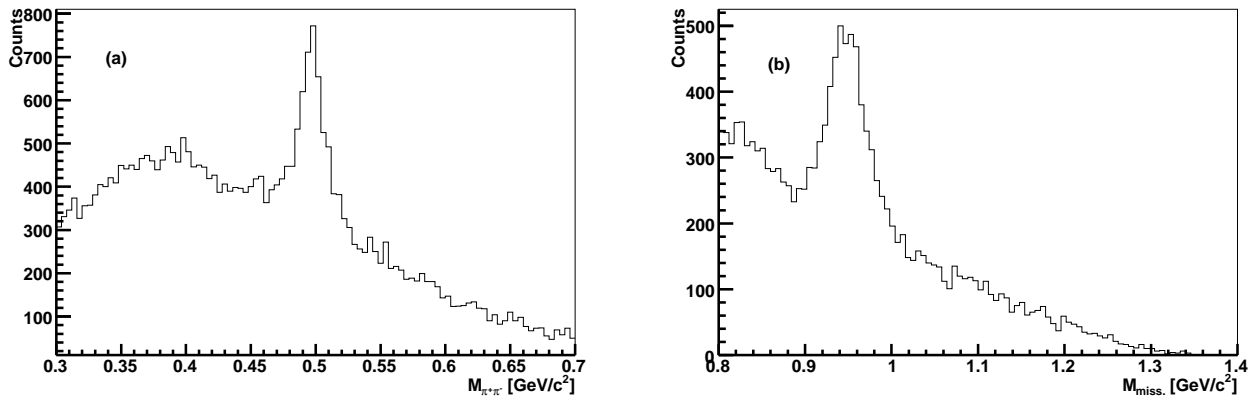


**Fig. 4.** Mass distributions for the reaction  $\gamma p \rightarrow K^+ K_S^0 n$ , (a) Invariant mass of  $\pi^+ \pi^-$  pairs in preselected 3-track data with  $K_S^0$ -peak. The following cuts were applied: for the neutron  $|M_{\text{miss}} - 0.94 \text{ GeV}| < 0.075 \text{ GeV}$  and for the  $K^+$  a TOF mass information of  $m > 0.3 \text{ GeV}$ . (b) Distribution of missing mass recoiling against the three tracks for all selected 3-track events showing a peak due to the missing neutron.

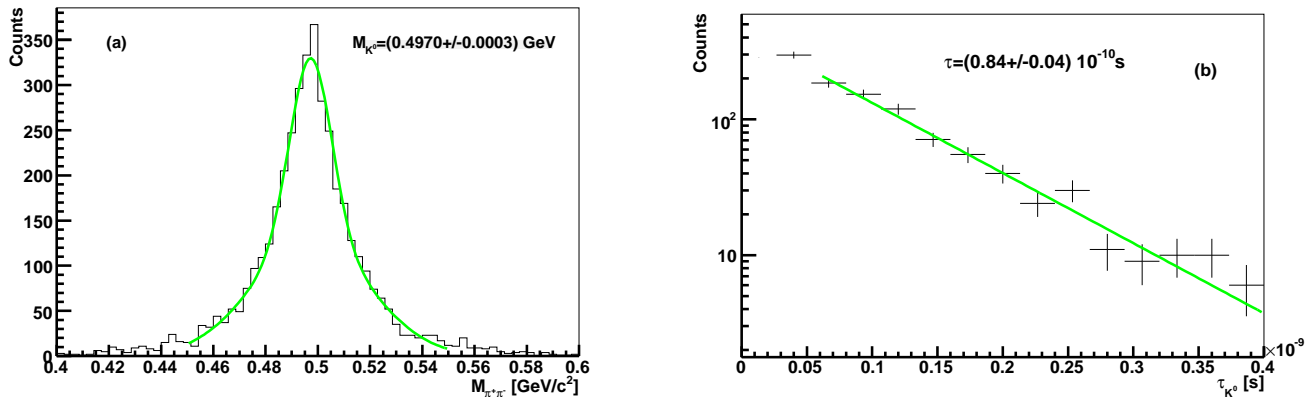


**Fig. 5.** (a) Invariant mass distribution of  $\pi^+ \pi^-$  pairs after complete selection procedure including a kinematical fit (see text), calculated from the measured 4-momenta and (b) decay time distribution of the  $K_S^0$  for selected events from the reaction  $\gamma p \rightarrow K^+ K_S^0 n$ .

tributions in four photon-energy bins with a double Voigt function and a background term (not shown).

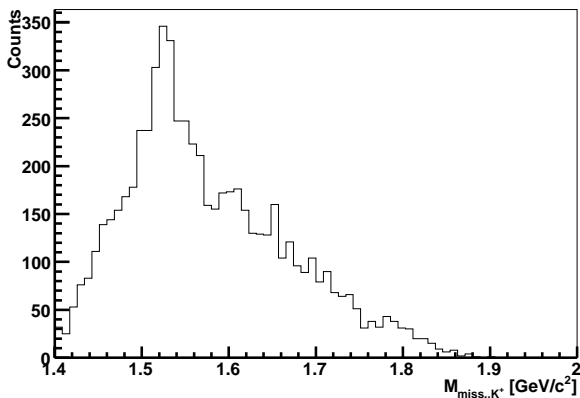


**Fig. 6.** Missing mass recoiling against the  $K^+$  showing the  $\Lambda(1520)$  peak.

### 3.3 $\Lambda(1520) \rightarrow \Sigma^\pm \pi^\mp$

The topologies of the reactions  $\gamma p \rightarrow K^+ \Sigma^- \pi^+$  with  $\Sigma^-$  decaying into  $n\pi^-$  and  $\gamma p \rightarrow K^+ \Sigma^+ \pi^-$  with  $\Sigma^+$  into  $n\pi^+$  and  $p\pi^0$  are shown in figs. 3 (b) and (c), respectively. First, the primary vertex was reconstructed in a fit of the intersection of tracks trying all possible pairs of charged particles. The vertex fit with the best fit probability was accepted. Then the  $\Sigma^\pm$  momentum was reconstructed at this vertex by a kinematic fit to hypotheses 3 and 4 (table 1). As next step, the decay vertex of  $\Sigma^\pm$  was reconstructed in a fit as intersection of the reconstructed  $\Sigma$  track with the third charged track. The  $\Sigma^\pm$  decay hypotheses were tested by a kinematic fit at the decay vertex. The  $K^+$  mass, determined from time-of-flight measurement had to lie in the region  $0.4 < M_{K^+} < 0.7 \text{ GeV}$ . In order to remove background from other reactions, further kinematic cuts were applied. The masses of  $n$  and  $\pi^0$  candidates, calculated as missing mass at the  $\Sigma$  decay vertex, had to be in the regions  $|M_{\text{miss}} - M_n| < 0.07 \text{ GeV}$

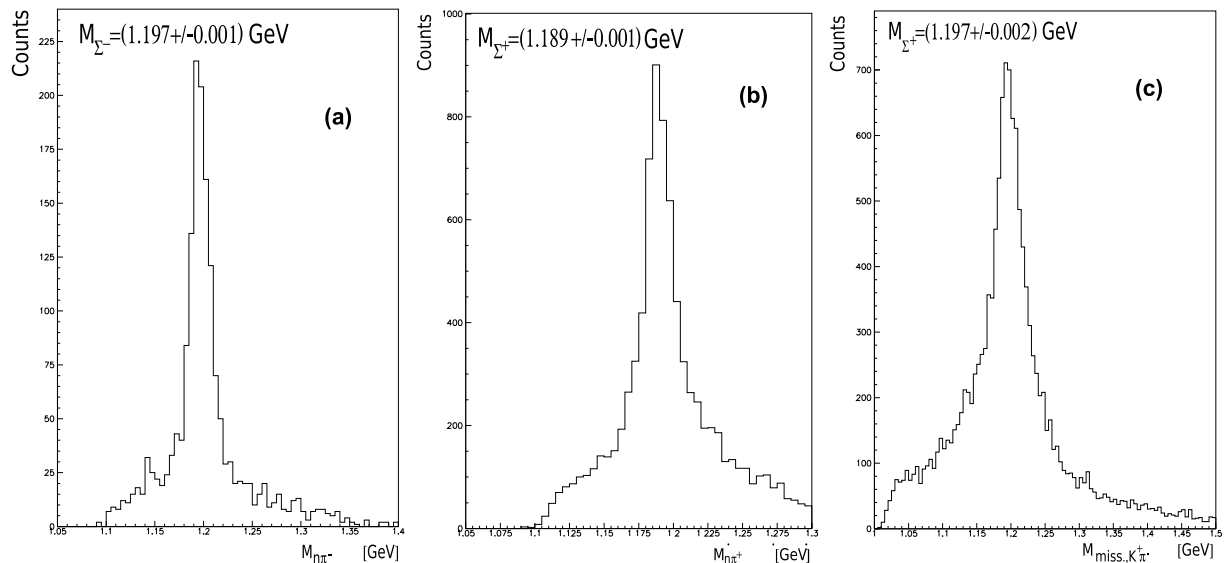


**Fig. 7.** (a) Invariant mass distribution  $M_{n\pi^-}$  of the  $n\pi^-$  system of the  $\Sigma^-$ -decay for selected events from the reaction  $\gamma p \rightarrow K^+ \Sigma^- \pi^+$ , (b) Invariant mass  $M_{n\pi^+}$  of the  $n\pi^+$  system of the  $\Sigma^+$ -decay for selected events from the reaction  $\gamma p \rightarrow K^+ \Sigma^+ \pi^-$ , (c) Missing mass  $M_{\text{miss}, K^+\pi^-}$  recoiling against the  $K^+\pi^-$  system for the decay-channel  $\Sigma^+ \rightarrow p\pi^0$ .

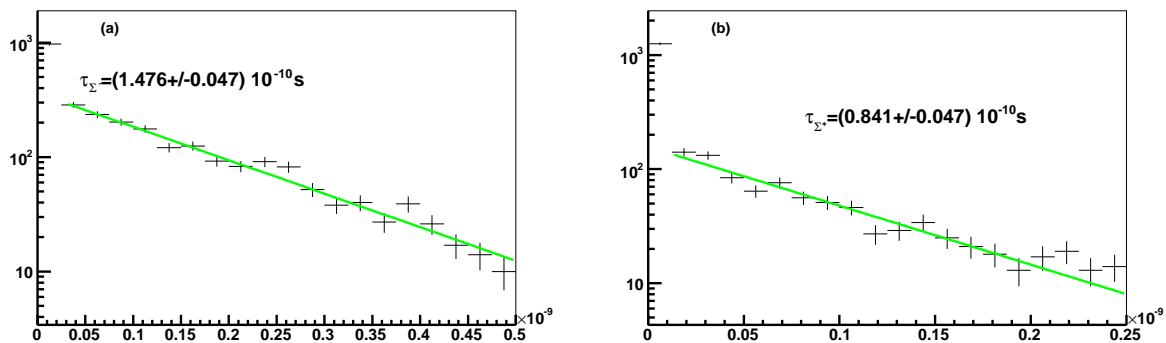


**Fig. 8.** (a) Decay time distribution of  $\Sigma^-$ , (b) Decay time distribution of  $\Sigma^+$ .

and  $|M_{\text{miss}}^2 - M_{\pi^0}^2| < 0.005 \text{ GeV}^2$ , respectively. The invariant mass of the  $n\pi^\mp$  system, calculated at the decay vertex, had to be in the range of the nominal mass of the  $\Sigma$  ( $|M_{n\pi^\pm} - M_{\Sigma^\pm}| < 0.017 \text{ GeV}$ ). For  $\Sigma^+ \rightarrow p\pi^0$ , it was requested that the missing mass recoiling against the  $K^+\pi^-$  system at the primary vertex is in the range  $1.165 < M_{\text{miss}, K^+\pi^-} < 1.229 \text{ GeV}$ . Remaining background from the reaction  $\gamma p \rightarrow nK^+ K_s^0$  was removed by requiring  $|M_{\pi^+\pi^-} - M_{K_s^0}| > 0.03 \text{ GeV}$ . In addition it was demanded that the  $K^+$  mass, as determined from time-of-flight measurement, was in the  $0.4 < M_{K^+} < 0.7 \text{ GeV}$  range.

For the decay  $\Sigma^+ \rightarrow p\pi^0$ , background events from the reaction  $\gamma p \rightarrow K^+ \Lambda \pi^0$  with  $\Lambda \rightarrow p\pi^-$  were removed by an anti-cut around the  $\Lambda$  mass ( $1.098 < M_{p\pi^-} < 1.128 \text{ GeV}$ ). Figure 7 shows the invariant mass distributions of (a)  $n\pi^-$  from the  $\Sigma^-$  decay, (b)  $n\pi^+$  from the  $\Sigma^+$  decay, and (c) the missing mass recoiling against the  $K^+\pi^-$  system for the decay channel  $\Sigma^+ \rightarrow p\pi^0$ . Figure 8 presents decay time distributions of  $\Sigma^-$  (a) and  $\Sigma^+$  (b) after the complete

event selection and kinematical fits. The mass and lifetime values are consistent with the PDG data.

Figure 9 shows the distributions of missing masses recoiling against the  $K^+$  for the reactions  $\gamma p \rightarrow K^+ \Sigma^- \pi^+$  (a) and  $\gamma p \rightarrow K^+ \Sigma^+ \pi^-$  (b). Again the distributions were fitted in four photon energy bins with a double Voigt function and a polynomial background term.

### 3.4 $\Lambda(1520) \rightarrow \Lambda \pi^+ \pi^-$

Events from the reaction  $\gamma p \rightarrow K^+ \Lambda \pi^+ \pi^-$ , where  $\Lambda$  decays into  $p\pi^-$ , were reconstructed from the photon energy and five charged tracks. The decay vertex of the  $\Lambda$  candidate was tentatively reconstructed as intersection of a positively charged track with each of the negative tracks, accepting the fit with the calculated invariant mass closest to the nominal  $\Lambda$  mass. The primary vertex was determined using the reconstructed  $\Lambda$  line of flight and the

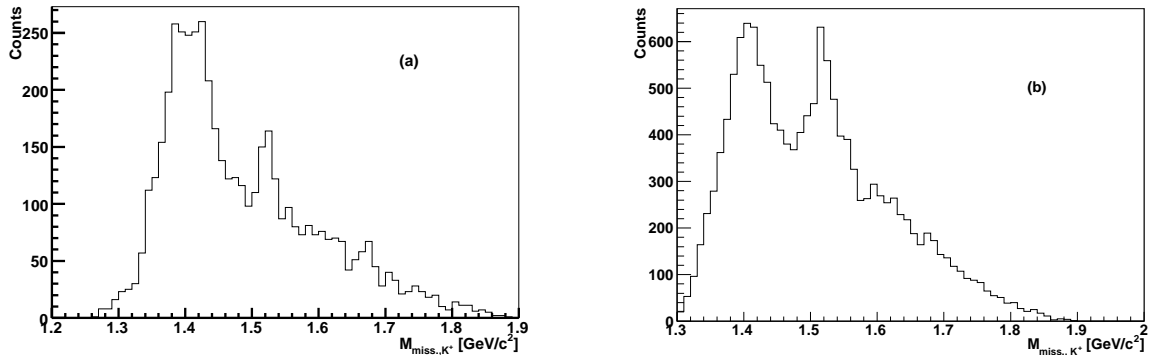


**Fig. 9.** (a) Missing mass distribution  $M_{miss,K^+}$  recoiling against the  $K^+$  for the reaction  $\gamma p \rightarrow K^+ \Sigma^- \pi^+$  with the peak of the  $\Lambda(1520)$  and a peak due to the  $\Sigma(1385)/\Lambda(1405)$  complex, (b) Missing mass distribution  $M_{miss,K^+}$  for the reaction  $\gamma p \rightarrow K^+ \Sigma^+ \pi^-$  (for both decay-channels of the  $\Sigma^+$ ) with peaks of the  $\Lambda(1520)$  and  $\Sigma(1385)/\Lambda(1405)$ .

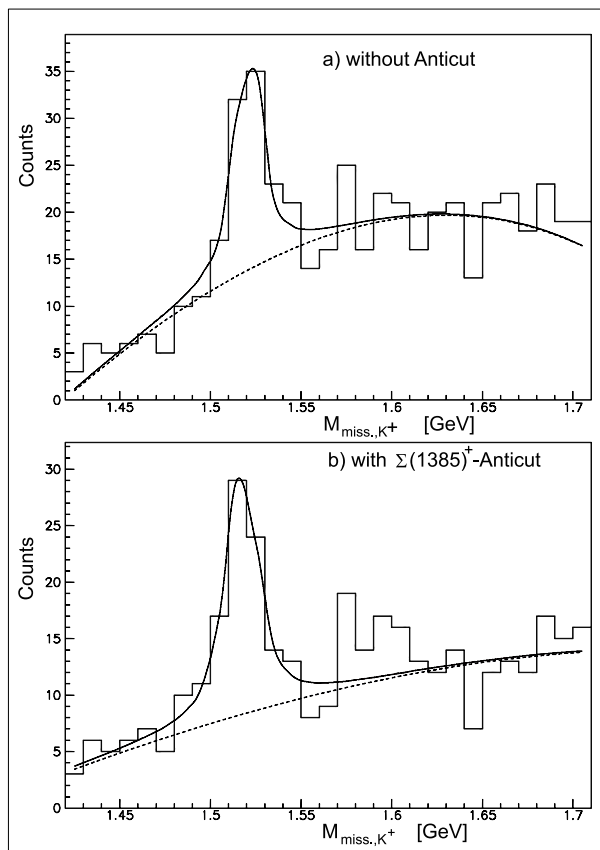


**Fig. 10.** Decay of  $\Lambda(1520)$ -hyperons in the channel  $\Lambda(1520) \rightarrow \Lambda \pi^+ \pi^-$ . Missing-mass distribution  $M_{miss,K^+}$  with the peak of the  $\Lambda(1520)$ -hyperon a) without further cuts, b) with an anticut in the region of the missing mass  $M_{miss,K^+ \pi^-}$  of  $\Sigma(1385)^+$  decays. Full lines describe the fit, dashed lines the background assumption.

remaining tracks. To reduce background from other reactions, several cuts were applied. The missing mass recoiling against  $K^+ \pi^+ \pi^-$  had to lie in the  $\Lambda$  mass region ( $1.075 < M_{miss} < 1.149$  GeV). The longitudinal momentum had to be conserved to better than 0.15 GeV. The  $K^+$  mass assignment obtained from the time-of-flight mea-

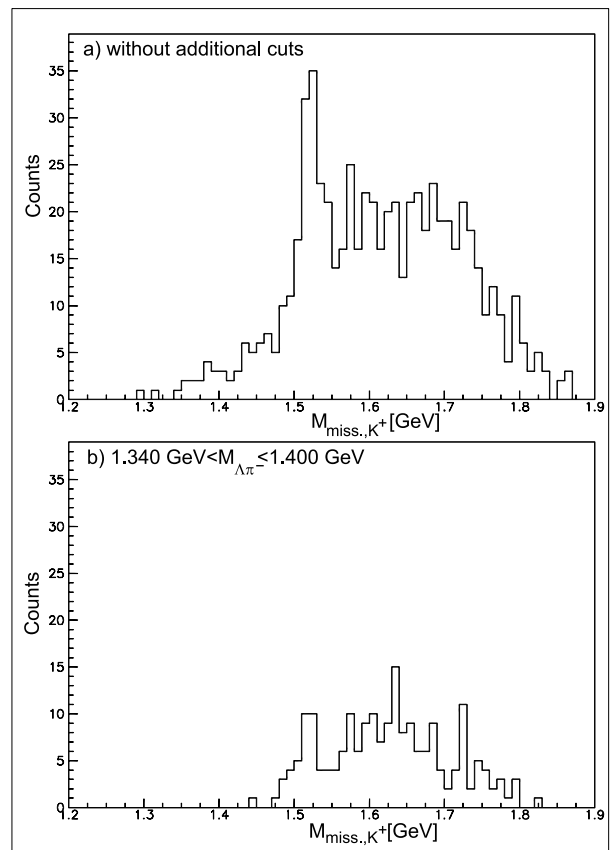


**Fig. 11.** Decay of  $\Lambda(1520)$ -hyperons in the channel  $\Lambda(1520) \rightarrow \Lambda \pi^+ \pi^-$ . Missing-mass distribution  $M_{miss,K^+}$  with the peak of the  $\Lambda(1520)$ -hyperon a) without further cuts, b) Missing mass plot of the  $\Lambda(1520)$ -hyperons with an invariant mass  $M_{\Lambda \pi^+ \pi^-}$  compatible with the decay channel  $\Lambda(1520) \rightarrow \Sigma(1385)^+ \pi^-$ .

surement had to be in the range  $0.4 < M_{K^+} < 0.7$  GeV. Finally a kinematic fit was used to select events of the wanted reaction. The distribution of the invariant mass opposite to  $K^+$  is shown in figs. 10 and 11. The number of  $\Lambda(1520) \rightarrow \Lambda \pi^+ \pi^-$  was determined as before.

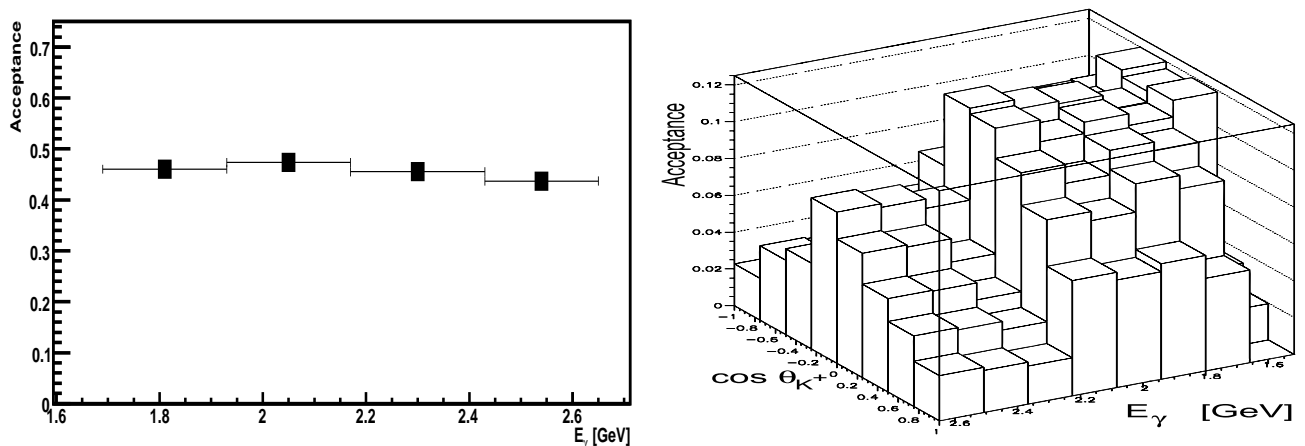


**Fig. 12.** Left panel: Acceptance of the reaction  $\gamma p \rightarrow K^+ \Lambda(1520)$  summed over the decay modes as a function of  $E_\gamma$ . Right panel: Acceptance for the reaction  $\gamma p \rightarrow K^+ K_S^0 n$  vs.  $E_\gamma$  and  $\cos \theta_{K^+}$ .

## 4 Background from other reactions

In order to estimate remaining background contributions which pass the selection process, background reactions (see table 1) were simulated according to phase space in the photon energy range of the data, and processed in the same way as real detector data. In addition to the reactions in table 1,  $\gamma p \rightarrow p\pi^+\pi^-\pi^+\pi^-$  and  $\gamma p \rightarrow p\pi^+\pi^-\pi^+\pi^-\pi^0$  were simulated for the  $\Lambda\pi^+\pi^-$  decay mode. The uncertainty in the shape of the background yield a total systematic uncertainty in the  $\Lambda(1520)$  cross section of less than 10% for all decay channels.

## 5 Acceptance

The acceptance was determined as a function of the photon energy  $E_\gamma$  and  $\cos \theta_{K^+}$  in the c.m.s. by means of Monte Carlo simulations using the GEANT programme package [9]. Events from the reaction  $\gamma p \rightarrow K^+ \Lambda(1520)$  with  $\Lambda(1520)$  decaying into the final states  $pK^-$ ,  $nK_S^0$ , and  $\Sigma^\pm \pi^\mp$  were generated by the SAGE-generator [10] with propagation of  $K_S^0$  and  $\Sigma^\pm$  according to their lifetimes and the decays  $K_S^0 \rightarrow \pi^+\pi^-$ ,  $\Sigma^- \rightarrow n\pi^-$ ,  $\Sigma^+ \rightarrow p\pi^0$ , and  $\Sigma^+ \rightarrow n\pi^+$ , respectively. Charged particles in the final states were tracked through the drift chamber system of the SAPHIR detector taking into account the magnetic field and multiple scattering in all materials passed. Simulated events were analyzed in the same way as real data. The determination of the acceptance comprised the trigger efficiency of the data taking periods, the event reconstruction efficiency and the efficiency of the selection process. On average the acceptance was of the order of 44% for  $\gamma p \rightarrow K^+ \Lambda(1520) \rightarrow K^+ pK^-$  and 8% for  $\gamma p \rightarrow K^+ K_S^0 n, K^+ \Sigma^\pm \pi^\mp$ . The reaction acceptance and, as an example, details for the  $K^+ K_S^0 n$  final state are given in fig. 12.

## 6 Results

### 6.1 Total cross section for $\gamma p \rightarrow K^+ \Lambda(1520)$

The number of  $\Lambda(1520)$  events was determined by fits to the  $pK^-$ ,  $nK_S^0$ ,  $\Sigma^-\pi^+$ , and  $\Sigma^+\pi^-$  mass distributions in five  $\cos \theta_{K^+}$  bins and for four bins in the photon energy covering the range from 1.69 GeV to 2.65 GeV. The fits were carried out assuming a Breit-Wigner form with a decay width fixed to the nominal value. Whilst in the  $nK_S^0$  and  $pK^-$  mass distributions only the  $\Lambda(1520)$  provided a narrow peak in the data, in the  $\Sigma\pi$  decay channels two additional Breit-Wigner functions for the  $\Sigma(1385)$  and  $\Lambda(1405)$  were necessary.

The total cross sections  $\sigma(E_\gamma)$  for  $\gamma p \rightarrow K^+ \Lambda(1520)$  determined from each decay channel was calculated from the number  $N_{\Lambda(1520)}(E_\gamma, \cos \theta_{K^+})$ , the acceptance  $A(E_\gamma, \cos \theta_{K^+})$ , the branching ratio  $BR$  and the global luminosity as the product of the photon flux  $N_\gamma(E_\gamma)$  through the target and the target area density  $\rho_T$ :

$$\sigma(E_\gamma) = \frac{1}{BR \cdot N_\gamma(E_\gamma) \rho_T} \sum \frac{N_{\Lambda(1520)}(E_\gamma, \cos \theta_{K^+})}{A(E_\gamma, \cos \theta_{K^+})},$$

the sum extending over the  $\cos \theta_{K^+}$  bins.

The results are shown in table 2. The quoted errors were calculated by adding in quadrature the statistical errors, the systematic uncertainties due to the parametrisation of the background underneath the  $\Lambda(1520)$  peak, and the branching ratios. The total cross sections of the reaction  $\gamma p \rightarrow K^+ \Lambda(1520)$  are shown in fig. 13. In fig. 13(a) cross sections for different decay channels are presented. In fig. 13(b) the results for the  $\Lambda(1520) \rightarrow K^- p$  decay channel determined by integration of  $d\sigma/dt$  (see section 6.2) is shown. The  $d\sigma/dt$  cross sections from the four decay channels were averaged and integrated. The results are also shown in fig. 13(b). The error bars indicate the errors of the fitting procedure only, the differences between the three methods indicate the magnitude of the systematic errors. The results are consistent within the error bars.

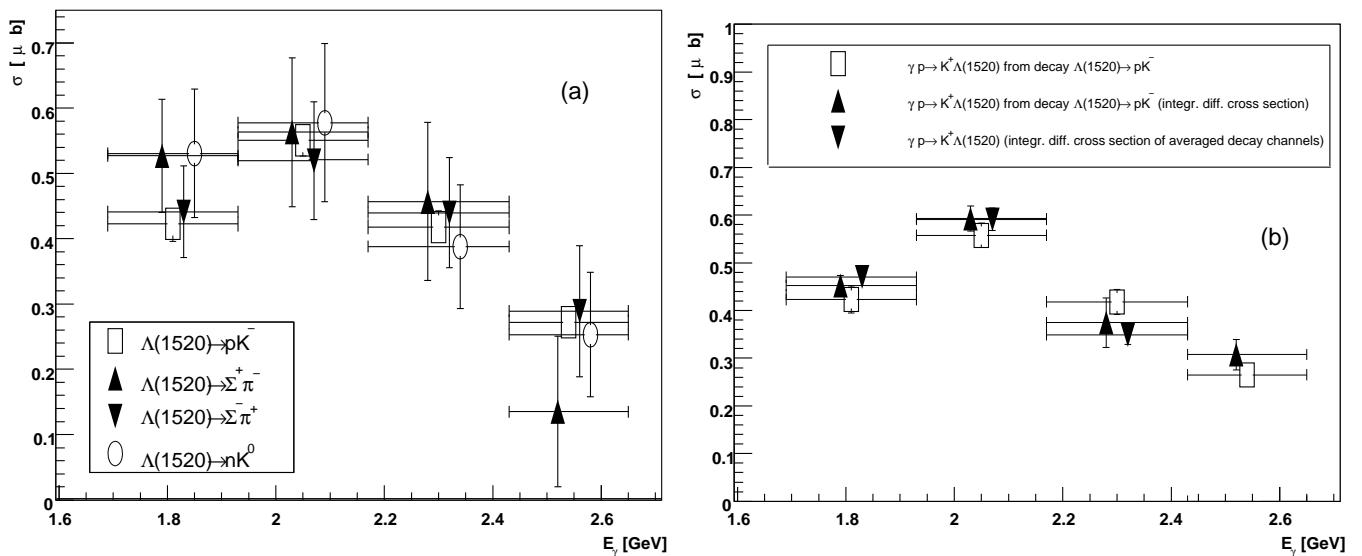


**Fig. 13.** (a) Total cross section for the reaction  $\gamma p \rightarrow K^+ \Lambda(1520)$  as determined in different decay channels, (b) Comparison of the total cross sections for the dominant decay channel  $\Lambda(1520) \rightarrow pK^-$  (see (a), squares) gained via integration of the differential cross sections  $d\sigma/dt$  (upward triangles), and the averaged and integrated differential cross sections (downward triangles) from the four decay channels presented in (a).

**Table 2.** Total cross section for the reaction  $\gamma p \rightarrow K^+ \Lambda(1520)$  determined in different decay channels of the  $\Lambda(1520)$ . The errors are largely due to the systematical uncertainty of the background parametrisation.

$E_\gamma$ [GeV]	$pK^-$ [ $\mu\text{b}$ ]	$\Sigma^+ \pi^-$ [ $\mu\text{b}$ ]
1.69–1.93	$0.422 \pm 0.031$	$0.518 \pm 0.084$
1.93–2.17	$0.503 \pm 0.033$	$0.564 \pm 0.113$
2.17–2.41	$0.418 \pm 0.029$	$0.456 \pm 0.118$
2.41–2.65	$0.270 \pm 0.031$	$0.139 \pm 0.115$

$E_\gamma$ [GeV]	$\Sigma^- \pi^+$ [ $\mu\text{b}$ ]	$nK^0$ [ $\mu\text{b}$ ]	average [ $\mu\text{b}$ ]
1.69–1.93	$0.442 \pm 0.070$	$0.532 \pm 0.097$	$0.442 \pm 0.026$
1.93–2.17	$0.519 \pm 0.088$	$0.577 \pm 0.118$	$0.482 \pm 0.029$
2.17–2.41	$0.439 \pm 0.083$	$0.389 \pm 0.098$	$0.420 \pm 0.026$
2.41–2.65	$0.297 \pm 0.096$	$0.254 \pm 0.088$	$0.242 \pm 0.027$

## 6.2 Differential cross sections

The differential cross sections  $d\sigma/dt$  of the reaction  $\gamma p \rightarrow K^+ \Lambda(1520)$  were determined for four photon-energy intervals. Invariant mass distributions were plotted in each energy and  $t$  interval and fitted in order to determine the number of produced  $\Lambda(1520)$  hyperons. The cross sections are shown in fig. 14 and table 3. In the four analyzed photon energy intervals the modulus of the exponential  $t$ -slope decreases from 5.4 to 1.5  $\text{GeV}^{-2}$  with increasing photon energies.

The differential cross sections  $d\sigma/d\cos\theta_{\text{GJ}}$  in the  $t$ -channel helicity frame (Gottfried-Jackson frame, fig. 15) were determined from the decay  $\Lambda(1520) \rightarrow pK^-$ , again in four photon energy bins (fig. 16).

**Table 3.** Differential cross sections and  $t$ -slopes for the reaction  $\gamma p \rightarrow K^+ \Lambda(1520)$  determined via the decay channel  $\Lambda(1520) \rightarrow pK^-$  in four photon energy bins. For the slopes estimates on the systematical errors are given.

$E_\gamma$ [GeV]	$t$ [ $\text{GeV}^2$ ]	$d\sigma/dt$ [ $\mu\text{b}/\text{GeV}^2$ ]	slope [ $\text{GeV}^{-2}$ ]
1.69–1.93	0.0–0.2	$1.547 \pm 0.077$	$-5.41 \pm 0.7$
	0.2–0.4	$0.386 \pm 0.046$	
	0.4–0.671	$0.219 \pm 0.029$	
1.93–2.17	0.0–0.2	$1.076 \pm 0.081$	$-2.20 \pm 0.3$
	0.2–0.4	$0.814 \pm 0.062$	
	0.4–0.6	$0.489 \pm 0.050$	
	0.6–1.285	$0.172 \pm 0.017$	
2.16–2.41	0.0–0.2	$0.419 \pm 0.057$	$-1.63 \pm 0.4$
	0.2–0.4	$0.496 \pm 0.058$	
	0.4–0.6	$0.385 \pm 0.039$	
	0.6–0.9	$0.196 \pm 0.025$	
	0.9–1.790	$0.063 \pm 0.092$	
2.41–2.65	0.0–0.3	$0.361 \pm 0.057$	$-1.51 \pm 0.4$
	0.3–0.6	$0.283 \pm 0.057$	
	0.6–0.9	$0.235 \pm 0.055$	
	0.9–1.60	$0.063 \pm 0.017$	

The  $t$ -channel helicity-frame  $z$ -axis is defined as antiparallel to the incident photon in the  $\Lambda(1520)$  rest frame, the  $y$ -axis being normal to the production plane. The angular distribution serves as an indicator in case of  $t$ -channel exchange. If the  $\Lambda(1520)$  ( $J^P = 3/2^-$ ) is produced with  $m_z = \pm 1/2$  indicating  $K^-$  exchange, one ex-



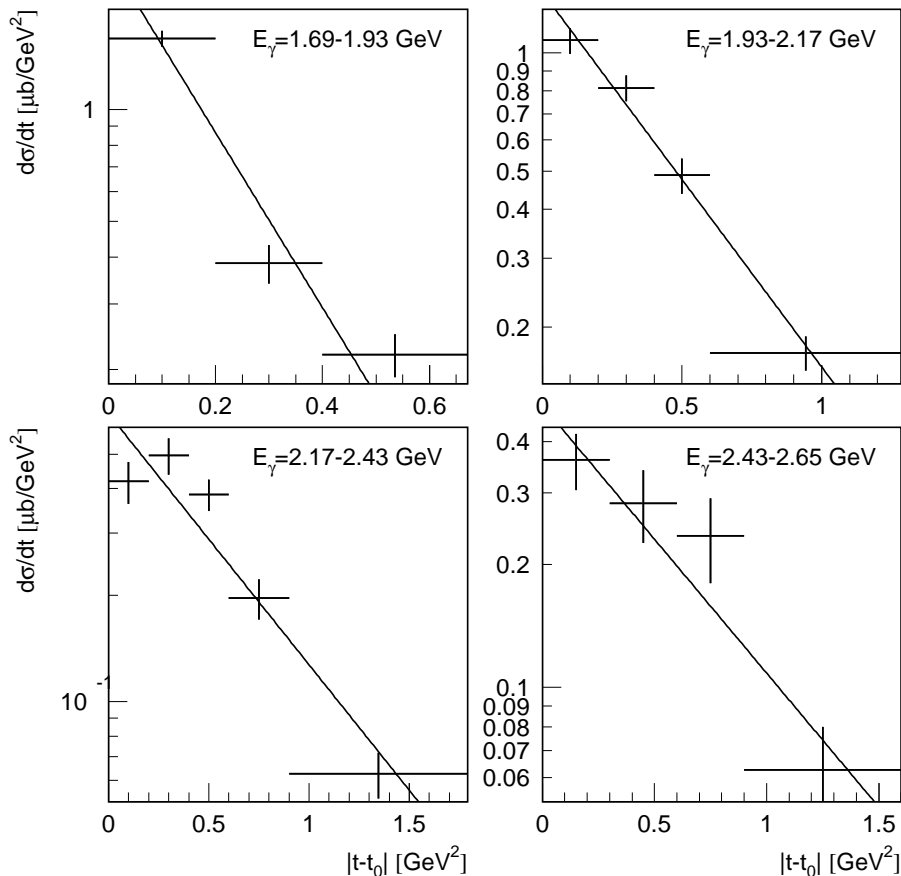


**Fig. 14.** Differential cross section for the reaction  $\gamma p \rightarrow K^+ \Lambda(1520)$  determined via the decay channel  $\Lambda(1520) \rightarrow pK^-$  in four photon energy bins as a function of  $|t - t_0|$ ;  $t_0$  denotes the minimal kinematically allowed squared four-momentum transfer, which was calculated on an event-by-event basis.

pects a  $1 + 3 \cos^2 \theta_{K^-}$  distribution, whereas a  $\sin^2 \theta_{K^-}$  distribution indicates  $K^*$  exchange with  $m_z = \pm 3/2$ . Published data from the LAMP2 Group [11] strongly favour a nearly exclusive production via  $K^*$  exchange. The elec-

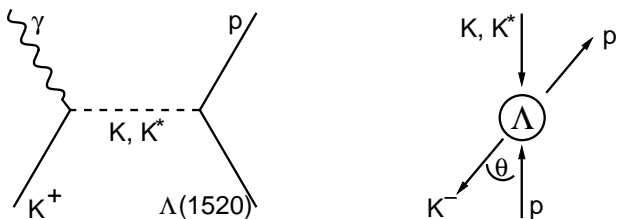


**Fig. 15.** The  $t$ -channel helicity (Gottfried-Jackson) frame for the  $\Lambda(1520)$ .

troproduction data from CLAS [1] are presented in four  $Q^2$  bins between 0.9 and 2.4  $\text{GeV}^2$  averaged over  $W$  from threshold to 2.43 GeV. In these data,  $K$  exchange dominates, in particular towards larger  $Q^2$  values. The authors [1] suggest that the difference to the LAMP2 results might be due to substantial contributions from longitudinally polarized photons. Our photoproduction results between  $E_\gamma = 1.69$  and 2.65 GeV do not show a preference for  $K^*$  or  $K$  exchange in the  $t$ -channel. We applied an  $\alpha(1 + 3 \cos^2 \theta_{K^-}) + \beta \sin^2 \theta_{K^-} + \gamma \cos \theta_{K^-}$  fit in order to take into account interference terms from the  $J = 1/2$  hyperon production background, as suggested by the CLAS group [1]. When the data are divided into four energy bins (fig. 16) a  $\sin^2 \theta_{K^-}$  dominance is observed at low energies. For energies above 2.43 GeV a  $1 + 3 \cos^2 \theta_{K^-}$  shape is seen which indicates that  $K$  exchange is clearly preferred. This

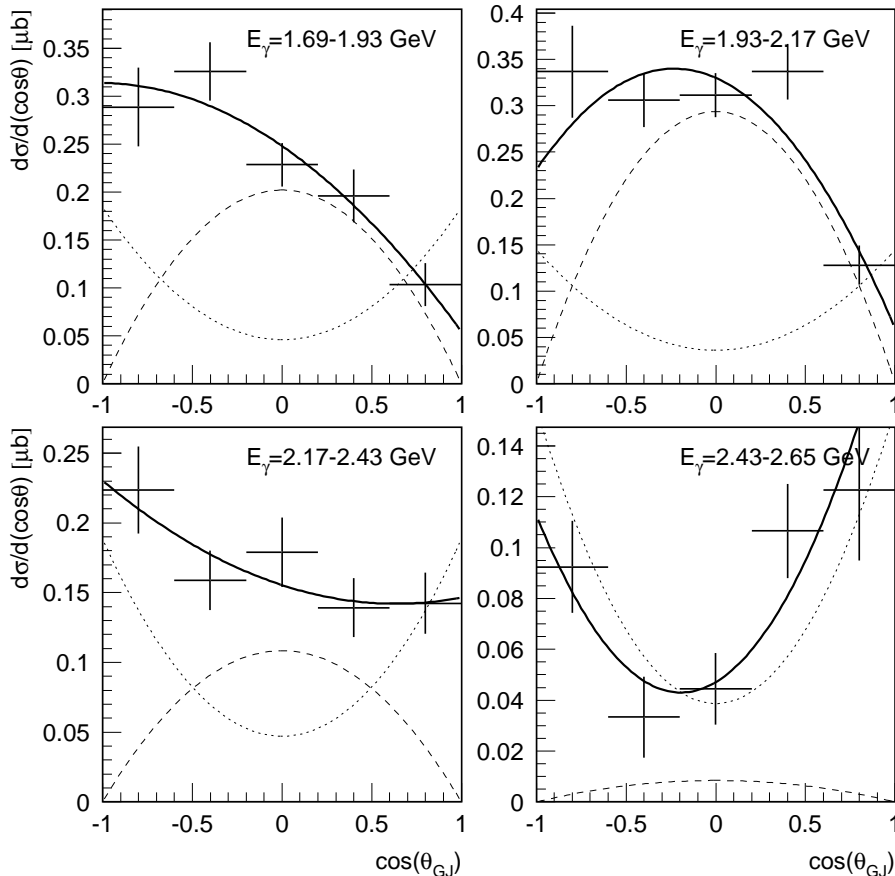


**Fig. 16.** The  $\Lambda(1520)$  decay angular distribution in four energy bins in the  $t$ -channel helicity system. Solid line: complete fit (see text), dashed line:  $1 + 3 \cos^2 \theta_{K^-}$  corresponding to  $K^*$  exchange, dotted line:  $\sin^2 \theta_{K^-}$  corresponding to  $K$  exchange.

is in contrast to the LAMP2 results, but seems compatible with the CLAS electroproduction data. The observed  $t$ -channel angular distribution changes rather rapidly with energy. Hence it cannot be assigned to variations in  $K^*$  or  $K$  exchange. Therefore we conclude that this is likely due to interference of  $t$ -channel exchange processes with amplitudes for resonances formed in the  $s$ -channel.

## 7 $\Lambda(1520)$ decays

### 7.1 Branching ratio for $\Lambda(1520) \rightarrow NK$ and $\Sigma\pi$

The total and differential cross sections presented in tables 2 and 3 are calculated using the  $\Lambda(1520)$  decay branching fractions [8]. In turn, the data allow us also to deduce the branching fractions, even though with larger errors. The values resulting from an integration of the efficiency

**Table 4.**  $\Lambda(1520)$  decay branching ratios.

Decay mode	PDG [8]	this work
$pK^-$	} $45 \pm 1\%$	$(23.4 \pm 1.6)\%$
$nK^0$		$(21.6 \pm 2.8)\%$
$\Sigma^+\pi^-$	} $42 \pm 1\%$	$(11.8 \pm 2.1)\%$
$\Sigma^0\pi^0$		-
$\Sigma^-\pi^+$		$(16.3 \pm 1.7)\%$

corrected event numbers are collected in table 4 and compared to PDG numbers. The ratios presented here are normalized to the sum of the fractions for decays into  $pK^- + nK^0$  and  $3/2(\Sigma^-\pi^+ + \Sigma^+\pi^-)$ , respectively. The branching ratios are consistent with isospin invariance. The  $\Sigma^-\pi^+$  and  $\Sigma^+\pi^-$  branching ratios are compatible with 25% probability.

## 7.2 The $\Sigma(1385)\pi$ contribution to $\Lambda\pi\pi$ in $\Lambda(1520)$ decays

The  $\Lambda\pi\pi$  decay channel is of special interest since the  $\Lambda(1520)$  might be a candidate for a  $\Sigma(1385)\pi$  molecule. In [12] it is argued that the  $\Lambda(1520)$  has a very strong coupling to the  $\Sigma(1385)\pi$  channel, while the small branching ratio into  $\Lambda\pi\pi$  is assigned to the small phase space of the decay into  $\Sigma(1385)\pi$ . With a strong coupling to  $\Sigma(1385)\pi$ , the  $\Lambda(1520)$  can be generated dynamically in a unitarized coupled-channel calculation.

Experimentally, the fractional contribution of  $\Sigma(1385)\pi$  in  $\Lambda(1520) \rightarrow \Lambda\pi\pi$  decays is not precisely known. Watson et al. [13] found that this contribution cannot be deduced reliably from their data. Mast et al. [14] analyzed bubble chamber events of the type  $K^- p \rightarrow \Lambda\pi^+\pi^-$  and found that  $0.82 \pm 0.10$  of the  $\Lambda\pi^+\pi^-$  decay proceeds via  $\Sigma(1385)\pi$ . From inelastic reactions of a  $K^-$  beam impinging on a neutron (in a  $D_2$  target), Corden et al. [15] determined this fraction to be  $0.58 \pm 0.22$ , while Burkhardt et al. [16] found  $0.39 \pm 0.10$ .

To determine this fractional contribution from the data presented here, we define  $\Sigma(1385)^\pm$  candidates by a  $1.34 \text{ GeV} < M_{\Lambda\pi^\pm} < 1.4 \text{ GeV}$  cut. For this purpose, the number of  $\Lambda(1520)$  hyperons in the missing mass distribution recoiling against the  $K^+$  is plotted in two ways (figs. 10 and 11): first without any additional cuts or anticuts, second with an anticut against the  $\Sigma(1385)$  candidates. The number of observed  $\Lambda(1520)$  hyperons is nearly unchanged (see fig. 10). In fig. 11 the number of events without and with a cut around the  $\Sigma(1385)$  mass is shown. The number of  $\Lambda(1520)$  hyperons is largely reduced by this cut. The remaining events may be due to the decay chain  $\Lambda(1520) \rightarrow \Sigma(1385)^\pm\pi^\mp$  or due to some background. We use the number of observed events as an upper limit for the ratio of  $\Lambda(1520)$  partial decay widths  $\frac{\Gamma(\Sigma(1385)^\pm\pi^\mp(\rightarrow\Lambda\pi^+\pi^-))}{\Gamma(\Lambda\pi^+\pi^-)}$ . We find this ratio to be less than 0.19 for a decay via  $\Sigma(1385)^-\pi^+$  and less than 0.25 for a decay via  $\Sigma(1385)^+\pi^-$ , yielding

$$\frac{\Gamma(\Sigma(1385)^\pm\pi^\mp(\rightarrow\Lambda\pi^+\pi^-))}{\Gamma(\Lambda\pi^+\pi^-)} < 0.44 \quad (90\% \text{ c. l.})$$

The result is hard to reconcile with the analysis of Mast et al. [14] or the predictions of Roca et al. [12].

## 8 Summary

Photoproduction of the  $\Lambda(1520)$  hyperon was studied from threshold to 2.65 GeV. The investigated decay channels were  $\Lambda(1520) \rightarrow pK^-$ ,  $\Lambda(1520) \rightarrow nK_s^0$ ,  $\Lambda(1520) \rightarrow K^+\Sigma^+\pi^-$ ,  $\Lambda(1520) \rightarrow K^+\Sigma^-\pi^+$ , and  $\Lambda(1520) \rightarrow \Lambda\pi^+\pi^-$ . We present total cross sections for  $\Lambda(1520)$  photoproduction obtained from the first four decay channels. The four cross sections are fully compatible. The differential cross section  $d\sigma/dt$  for  $\Lambda(1520) \rightarrow pK^-$  is shown in four energy bins. For this channel angular distributions in the  $t$ -channel helicity system (Gottfried-Jackson system) were

evaluated. Contrary to the LAMP2 [11] results our measurements do not support dominance of  $K^*$   $t$ -channel exchange. The results seem to be more compatible with the CLAS [1] electroproduction data. Therefore we cannot support the conjecture of the CLAS collaboration that the difference to the LAMP2 data might be due to the contribution of longitudinally polarized photons. So, the deeper reason for the discrepancy with the LAMP2 data has still to be understood, even taking into account that the LAMP2 data were measured under different kinematical conditions. The investigation of the  $\Lambda(1520) \rightarrow \Lambda\pi\pi$  channel shows no indication for a dominant decay via  $\Sigma(1385)\pi$ .

## 9 Acknowledgements

We would like to thank the technical staff of the ELSA machine group for their invaluable contributions to the experiment. We gratefully acknowledge the support by the Deutsche Forschungsgemeinschaft in the framework of the Schwerpunktprogramm ‘‘Investigation of the hadronic structure of nucleons and nuclei with electromagnetic probes’’ (SPP 1034 KL 980/2-3) and the Sonderforschungsbereich SFB/TR16 (‘‘Subnuclear Structure of Matter’’).

## References

1. S. P. Barrow *et al.* [Clas Collaboration], Phys. Rev. C **64**, 044601 (2001).
2. D.P. Barber *et al.* : Z. Physik C, Particles and Fields, 17-20 (1980).
3. I. Schulday *et al.*, accompanying paper.
4. W. J. Schuille *et al.*, The SAPHIR Collaboration, Nucl. Instr. Meth. A 344, 470 (1994).
5. D. Husmann, W. J. Schuille, Phys. Bl. 44, 40 (1988).
6. J. Barth *et al.*, Eur. Phys. J. A, 18, 117 (2003).
7. K.-H. Glander *et al.*, Eur. Phys. J. A 19, 251 (2004).
8. K. Nakamura *et al.* [Particle Data Group], J. of Phys. G37, 075021 (2010).
9. GEANT – CERN Program Library Long Writeup W5013, CERN Program Library Office.
10. R. B. Chaffee, A User’s Guide for SAGE, SLAC Computation Group Technical Memo No. 195 (1979) (unpublished).
11. D. P. Barber *et al.*, Z. Physik C, Particles and fields 7, 17 (1980).
12. L. Roca, Sourav Sarkar, V. K. Magas and E. Oset, Phys. Rev. C 73 045208 (2006).  
L. Roca, C. Hanhart, E. Oset and U.-G. Meissner, Eur. Phys. J. A27, 373-380 (2006).
13. M. B. Watson, M. Ferro-Luzzi and R. D. Tripp, Phys. Rev. **131**, 2248 (1963).
14. T. S. Mast, M. Alston-Garnjost, R. O. Bangerter, A. Barbaro-Galtieri, F. T. Solmitz and R. D. Tripp Phys. Rev. D **7**, 5 (1973).
15. M. J. Corden, G. F. Cox, A. Dartnell, I. R. Kenyon and S. W. O’Neale, Nucl. Phys. B **84**, 306 (1975).
16. E. Burkhardt *et al.*, Nucl. Phys. B **27**, 64 (1971).